# Chapter 1

Enhanced ECal reconstruction

The current implementation of the ECal reconstruction software was designed to reconstruct particles which originate from the ND280 tracker and enter the ECal. As section **??** shows, this was realised by only considering reconstructed ECal clusters under the single track-like or shower-like hypothesis. It should be evident that a neutrino interaction occurring within the ECal does not well fit this topology. While it is true that there is some power in the current reconstruction to distinguish a neutrino interaction from an entering track or shower, there is little feature information available. How many final state particles propagated from the interaction? How much visible energy was deposited by each of the particles? Where in the ECal did the interaction occur? These basic questions can not be trivially answered when using the current reconstruction. To maximise the ability of distinguishing ECal neutrino interactions from entering backgrounds, the reconstruction must be revisited.

1.1 The Hough transform

The Hough transform is a popular method of machine pattern recognition used by, but is not limited to, high energy physics experiments. Originally designed for machine track recognition in bubble chamber pictures [1], the version most widely used throughout the world was developed in 1972 [2]. The Hough transform is used to isolate specific features or shapes from a digital image. The simplest implementation, which is of most interest in event reconstruction, allows the extraction of straight 2D lines from a complex pattern. This is achieved by exploitation of a simple, but remarkable, feature of 2D geometry.

(a) Line in 2D Cartesian space.   **(b)** Point in 2D parameter space.
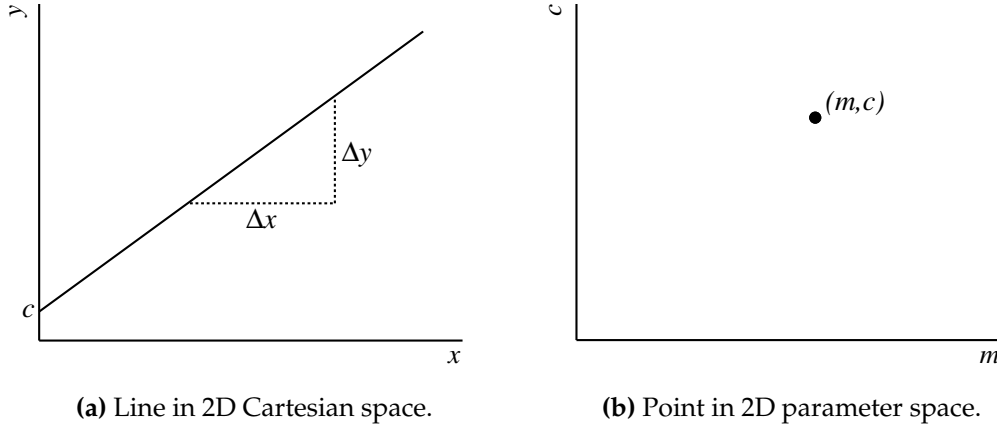
Figure 1.1: Representations of a 2D line in Cartesian space.

1.1.1 Line-point duality

Consider a straight line formed in a 2D Cartesian space as shown in Fig. 1.1a. The line
is usually described by

$$y = mx + c \tag{1.1}$$

where y and x are used as coordinates, m is the gradient of the line and c is the intercept
location of the line with the y axis. While it is not necessary to analyse this simple
shape in great detail, it is important to note that m and c are the only parameters
necessary to completely describe the line.

Now consider a new 2D space where the axes are defined by m and c, rather than x and
y (hereafter referred to as the parameter space). As this parameter space is described
by the parameters of a general 2D Cartesian line, there is an underlying symmetry
between the two spaces. The parameters of the 2D line shown in Fig. 1.1a can be used
to form a pair of coordinates (m,c) in the parameter space as shown in Fig. 1.1b. It is
important here to state clearly the general result; a straight line in Cartesian space is
represented by a single point in parameter space.

Now consider the 2D Cartesian space again. Unlike before, we will define a sin-
gle point rather than a straight line. Such a point is traditionally described by a pair
of coordinates (x,y). However, an alternative description of the point is an infinite
number of lines all of which pass through (x,y). This is highlighted by Fig. 1.2a where

(a) Point in 2D Cartesian space.   **(b)** Line in 2D parameter space.
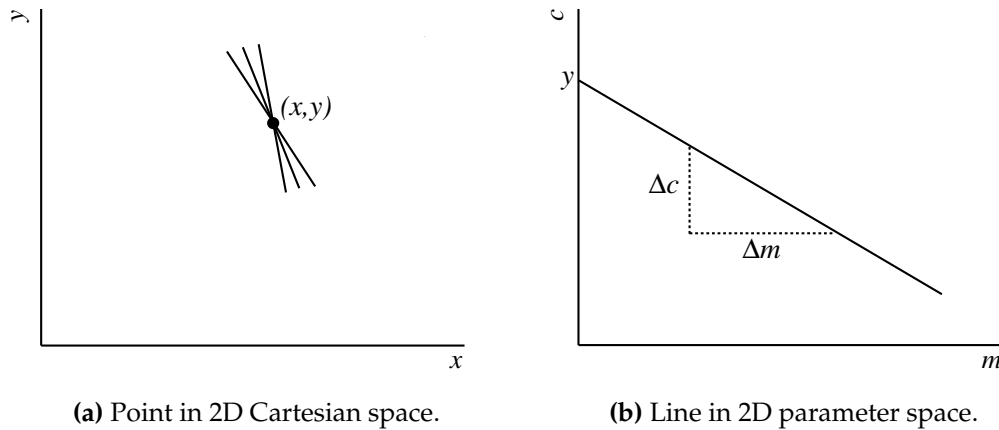
Figure 1.2: Representations of a 2D point in Cartesian space.

three lines of the infinite set are shown along with the point they represent. As the infinite line set are used to describe a single point, all lines in the set must follow a pattern. This relationship is revealed by simple algebraic manipulation of equation 1.1 to give

$$c = -xm + y. \tag{1.2}$$

Despite the manipulation, equation 1.2 still resembles the equation of a 2D line; however,[1] the parameters are x and y and the coordinates are m and c. Specifically, equation 1.2 is represented by a line in the parameter space defined above. The gradient of this line is

$$x = \frac{\Delta c}{\Delta m} \tag{1.3}$$

and the intercept of the line with the c axis is y as shown in Fig. 1.2b. As before, it is important to clearly state what has been shown; a point in Cartesian space is represented by a line in parameter space.

1.1.2 The parameter space

As section 1.1.1 shows, there is a clear relationship between the Cartesian space and the parameter space. Specifically, there is a symmetry between lines and points contained

---

[1]ADDRESSED - was ", however"; see http://www.nationalpunctuationday.com/semicolon.html
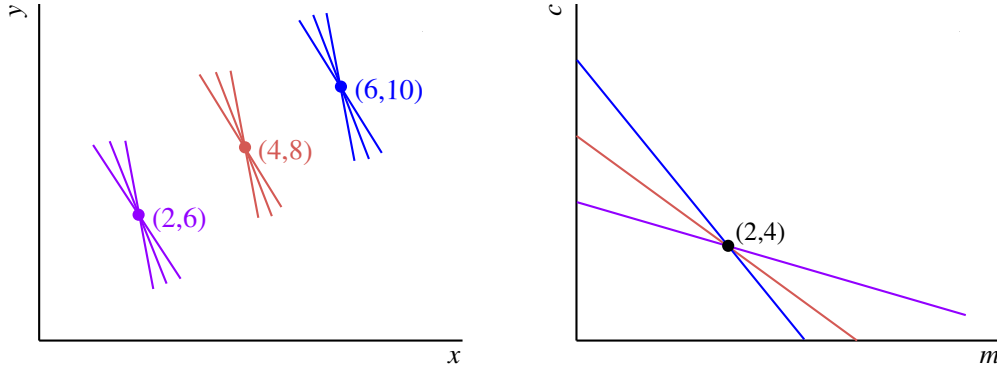
(a) The three Cartesian points defined in equation 1.4.

(b) The three parameter lines defined in equation 1.5. The coordinates (2,4) define the point of intersection of the three lines.

Figure 1.3: The three points defined in equation 1.4 and their representation in the parameter space. The colour coding matches the Cartesian points to their respective parameter lines.

in the two spaces. This relationship between the Cartesian and parameter spaces is not only interesting but also very powerful. Consider again the parameter line defined by equation 1.2 and shown in Fig. 1.2b. As shown in section 1.1.1, equation 1.2 was derived by considering the infinite set of lines which pass through a Cartesian point. As this infinite set represents the parameter line, it must also be true that the parameter line represents the infinite line set. Using one of the results from section 1.1.1, any point along the parameter line represents one of the lines from our infinite set. This key feature of the parameter space is the central component of the Hough transform.

We will now return to the Cartesian space for an example of how the Hough transform works. Let's define three points in this space,

$$
\begin{aligned}
p_1 &: (2, 6) \\
p_2 &: (4, 8) \\
p_3 &: (6, 10).
\end{aligned}
\tag{1.4}
$$

The three points defined in equation 1.4 are shown in Fig. 1.3a. Using one of the results from section 1.1.1 and equation 1.2, the three points can be Hough transformed
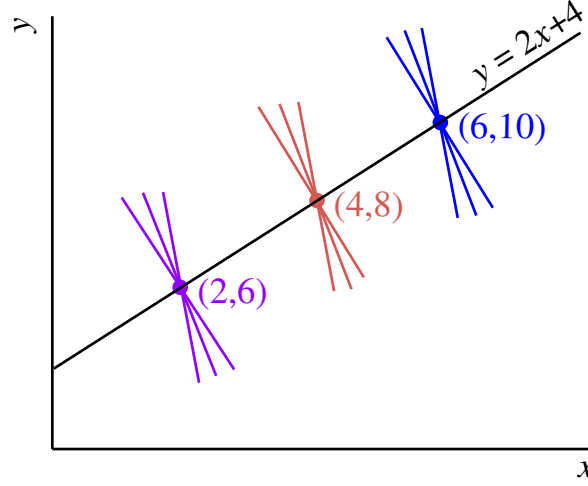
Figure 1.4: The line represented by the intersection in Fig. 1.3b with the Cartesian points it intercepts.

into the following parameter lines:

$$c = -2m + 6$$
$$c = -4m + 8 \qquad (1.5)$$
$$c = -6m + 10.$$

The three parameter lines are shown in Fig. 1.3b. From Fig. 1.3b, it is clear that the three parameter lines all cross at a common point with parameter space coordinates (2,4). Using the results from section 1.1.1, this common point in parameter space is represented by a line in Cartesian space. In addition, as (2,4) is common to all three parameter lines, the Cartesian line represented by (2,4) must also pass through all three Cartesian points defined by equation 1.4. This new Cartesian line is defined by

$$y = 2x + 4 \qquad (1.6)$$

and is shown in Fig. 1.4 with the original points used to generate the parameter lines. While this example is relatively simple, it demonstrates the capability of the Hough transform to recognise linear patterns in sets of points.
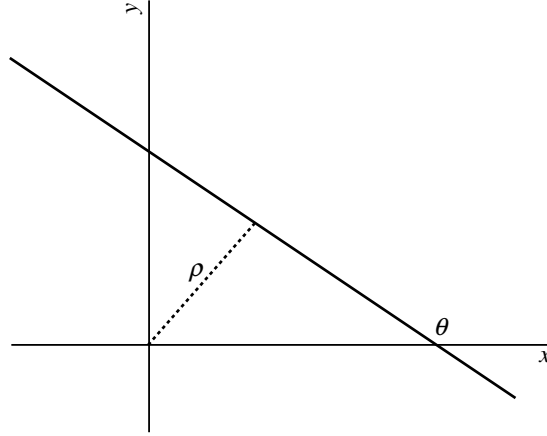
Figure 1.5: $\theta - \rho$ parameterisation of a 2D line.

1.1.3 Redefinition of parameters

Unfortunately, a complication in computation arises when $m \to \infty$. However, this complication can be removed by redefining the line parameters such that one is bounded. An alternative 2D line parameterisation is to specify a line in terms of the angle it makes with the x axis, θ, and the perpendicular distance of the line from the origin, ρ, as illustrated in Fig. 1.5. The functional form of the Cartesian line becomes

$$y = x\tan\theta + \frac{\rho}{\cos\theta}. \tag{1.7}$$

Using this new parameterisation, we must also define a new parameter space with axes θ and ρ. Using equation 1.7, a line in this new parameter space is defined by

$$\rho = y\cos\theta - x\sin\theta. \tag{1.8}$$

By definition, the θ axis of the parameter space must be bounded to the interval $[0,2\pi]$. If the directionality of the line is meaningless to the analyser, then the interval can be restricted to $[0,\pi]$.

The disadvantage of this parameterisation is that parameter line generation now involves trigonometric calculations which can be computationally expensive. However, this problem is small when compared to the unbounded complication of the traditional parameterisation.
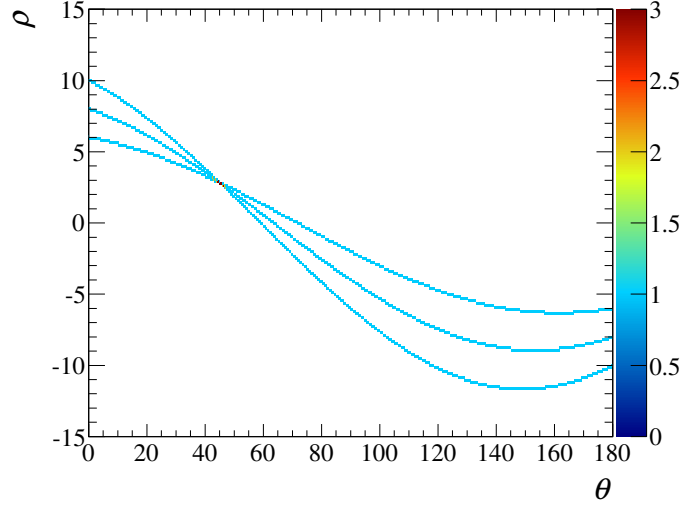
Figure 1.6: The discrete $\theta - \rho$ space. The plotted lines are those defined in equation 1.5 and reparameterised using equation 1.8.

1.1.4 Discretisation of the parameter space

It must now be considered how the parameter space is analysed. When a large number of parameter lines are generated, it becomes computationally expensive to analyse the resultant parameter space. While approaches exist to analyse the parameter space with very high precision [3], it is often only necessary to extract parameters with finite resolution. In such a case, it is convenient to discretise the parameter space. Under this regime, the parameter space is split into $\theta - \rho$ bins. Then, a parameter line is generated by incrementing the value of each $\theta - \rho$ bin it passes through. After each line has been added to the parameter space, the crossing locations can be readily found by searching for the $\theta - \rho$ bins with content larger than unity. An example of this discretisation is illustrated in Fig. 1.6, where the parameter lines defined in equation 1.5 have been re-parameterised using equation 1.8. The content of each bin in Fig. 1.6 records how many of the three parameter lines pass through each bin. The bin with value 3 is the crossing point of the three parameter lines.
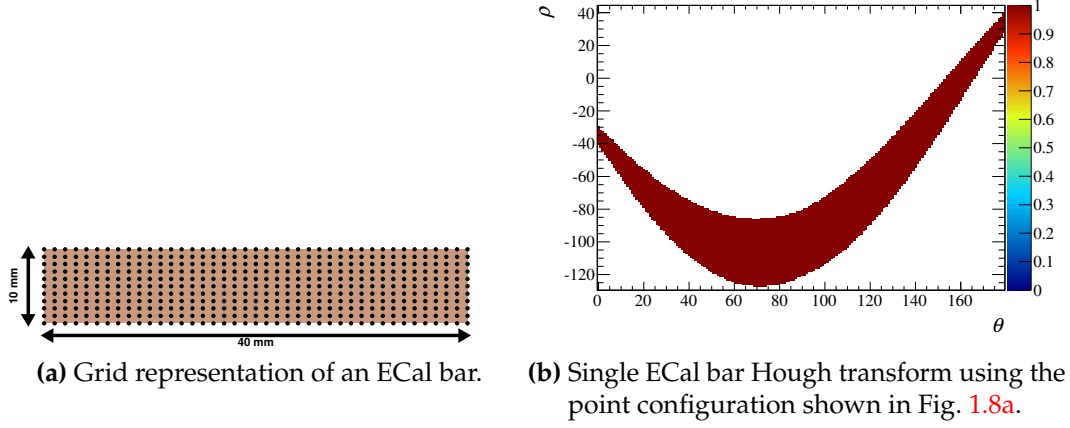
If a discretised approach is acceptable, which is the case in event reconstruction, construction and analysis of the parameter space is reduced to filling a 1D array N times, where N is the number of parameter lines, followed by a 1D grid search of the array to find the bin with the highest content.
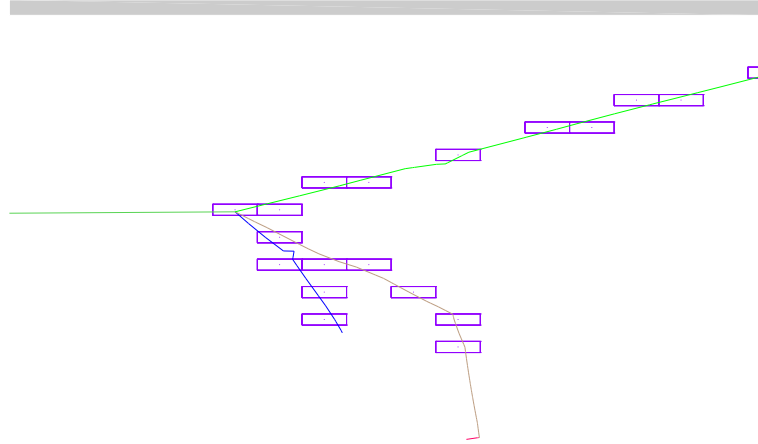
Figure 1.7: Simulated neutrino interaction with 3 final states in the side-right ECal. The green line entering from the left is the ν_μ. The green line exiting to the right is a μ^-, the brown line is a π^+ and the blue line is a proton. The purple rectangles represent the hit ECal bars.

1.2 ECal application of the Hough transform

We must now address how the Hough transform can be used as a reconstruction tool in the ECal. To do this, let's consider a neutrino interaction which occurs in the ECal as illustrated in 1.7. While the propagating neutrino is invisible to the ECal, the charged final state are definitely not. To first order, the final state particles propagate in straight lines depositing energy in the scintillator bars as they go. From this, we can infer that the hit bars arranged in straight lines should reveal the trajectory of the final states. As shown above, the Hough transform is capable of identifying straight lines from a set of coordinates. However, there are two complications in the ECal which the above sections have not addressed. We have only specifically discussed how to extract a single straight line from a pattern. As Fig. 1.7 shows, the number of final states can be, and is often, greater than one. This is merely a problem of computation which will be addressed in section 1.2.3. A much more severe problem is that the above demonstrations only deal with patterns constructed from infinitesimal points. While the centre of a scintillator bar can be used as a point for parameter line generation, it is unlikely that a final state particle will pass through the central point of the scintillator bars that it propagates through. If this is not addressed, the Hough transform will be of little use in trajectory reconstruction.

(a) Grid representation of an ECal bar.

(b) Single ECal bar Hough transform using the point configuration shown in Fig. 1.8a.

Figure 1.8: The grid representation of an ECal bar and its representation in parameter space.

1.2.1 Modelling the ECal bar

To make the Hough transform viable as a reconstruction tool, the finite dimensions of the ECal bar need to be incorporated into the parameter space generation. This feature of the ECal bars would be very problematic if the parameter space was continuous. However, it is only necessary to know the line parameters with finite resolution and a discrete parameter space can be used. This means that the ECal bar can be modelled as a set of Cartesian points and each of said points can be Hough transformed in turn to build up the parameter line representation of the ECal bar.

There are now two steps to consider. Firstly, how should the points be arranged? Remember that the Hough transform of a point represents all of the lines that pass through that point. So, the points should be arranged in such a fashion that any line which passes through the 2D cross-section of the ECal bar also has to pass through one of the points in the configuration. Secondly, the spacings between the points should be small enough that no gaps appear in the generated parameter line.

Assuming that every bin of the parameter space will have a $1° \times 1$ mm area, an obvious choice would be to use a rectangular grid of points with 1 mm spacing superimposed over the 2D cross-section of an ECal bar. The total number of points used to model the ECal bar is 451. To Hough transform the ECal bar, every point in the grid array can be Hough transformed individually with care taken to ensure that each $\theta - \rho$ bin is filled exactly once. The result is illustrated in Fig. 1.8b. The finite size of the ECal bar is evident by the finite size of the resultant parameter line.

While the generated parameter line accurately represents every line which passes through the ECal bar, there are two problems with this approach. Firstly, the large number of points to be Hough transformed is very large which results in a long CPU time. Secondly, there is a very high number of redundant calculations involved in the parameter line generation. Consider an exactly vertical line which passes through one of the points in the grid array. This line also passes through 10 other points in the same column of the grid. This means that when the parameter line is being generated, this vertical line is calculated 11 times for each column. Bearing this in mind, there are many points along the parameter line which are repeatedly calculated and provide no extra information. This would mean that any algorithm which uses this approach would be very CPU inefficient.
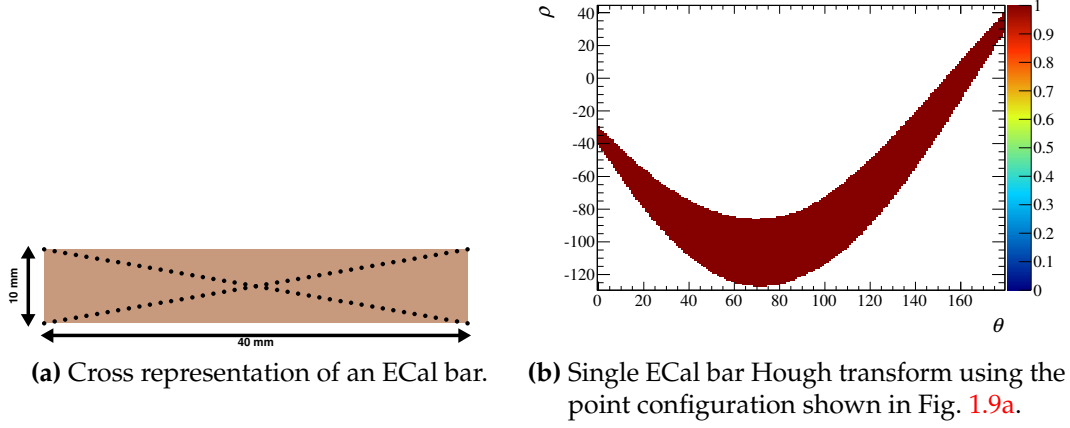
An alternative is to model the ECal bar as a set of points arranged in a cross as shown in Fig. 1.9a. Assuming that the spacing between the points on each line of the cross is infinitesimal, any line which passes through the ECal bar would also have to pass through one of the points in the configuration. As the parameter space is discrete, the spacing between the points need not be infinitesimal but only small enough to ensure that no gaps appear in the parameter line. Using 45 points on each line of the cross, the ECal bar can be Hough transformed by Hough transforming each point in the cross configuration. An example of this result is shown in Fig. 1.9b using the same ECal bar used to generate Fig. 1.8b. Clearly, Fig. 1.8b and Fig. 1.9b are identical showing that the cross model achieves the same result as the grid model. Comparing the two, the cross model uses a 90 point representation whereas the grid model uses a 451 point representation. This should mean that an algorithm utilising the cross model would be a factor of five faster than one using a grid model.

1.2.2 Parameter space generation

As we have addressed how to Hough transform an ECal bar, we are now in suitable position to generate the full parameter space for an ECal cluster. As described in section 1.1.3, the parameterisation of the 2D lines requires some point in space to act as the origin. It is possible to use the origin defined by the global ND280 geometry; however,[2] this is located in TPC 1 which would mean ρ will usually be the order of

---

[2]ADDRESSED - was ", however"

(a) Cross representation of an ECal bar.

(b) Single ECal bar Hough transform using the point configuration shown in Fig. 1.9a.

Figure 1.9: The cross representation of an ECal bar and its representation in parameter space.

metres. It is more convenient to define an origin in the vicinity of the ECal cluster being reconstructed. A simple option is to use the charge-weighted centre of the ECal cluster as the origin of the Hough transform. This location is simple to calculate and generally keeps ρ small.

The provided description of the Hough transform in all previous sections is strictly defined in 2D and so the ECal cluster should be split in such a way that this definition can be used. Fortunately, a 3D ECal cluster is built up using the two 2D views that the scintillator layers provide. So, it is relatively easy to split the 3D cluster into a pair of 2D clusters by collecting the cluster's hits into their respective 2D views.

We can now partly answer one of the problems raised in section 1.2 which is how to handle the track multiplicity aspect of the reconstruction? This is partly addressed by generating N parameter spaces with the same $\theta - \rho$ bin configuration where N is the number of hits in the 2D cluster. Each of the N parameter spaces will hold one parameter line generated by one of the 2D hits (in a similar fashion to Fig. 1.9b). The final parameter space can then be generated by adding together each of the N parameter spaces. The parameter space of the 2D cluster in Fig 1.7 is shown in Fig. 1.10.
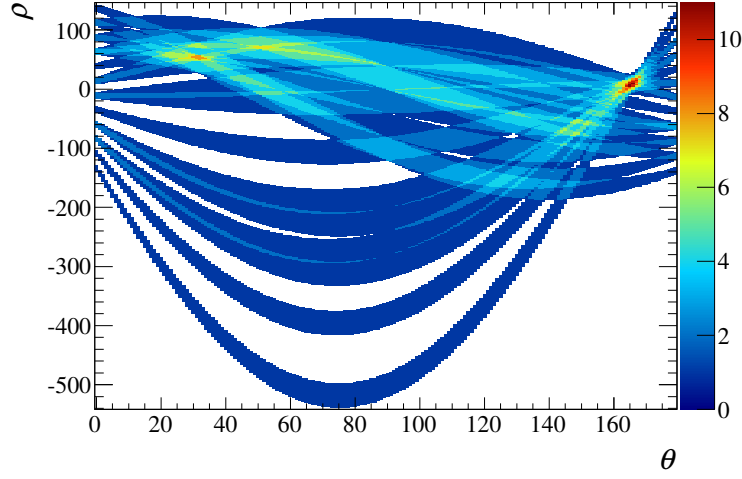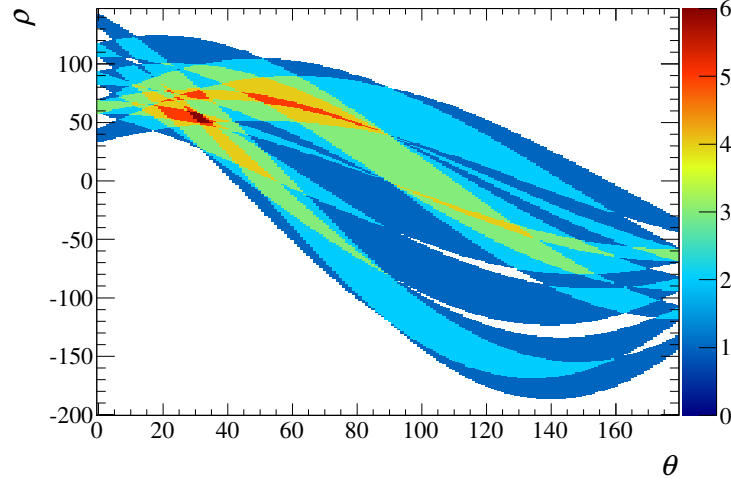
Figure 1.10: The full parameter space of the 2D cluster shown in Fig. 1.7.

1.2.3 Parameter space analysis

The full parameter space can look arbitrarily complicated. However, it contains a vast amount of trajectory related information about the cluster. Every $\theta - \rho$ bin of the parameter space describes a 2D track and the content value of said bin describes how many 2D ECal hits the track passes through. As described in section 1.2, a particle's trajectory should be straight in the ECal which means that the particles path should be revealed by finding the most hits arranged in a line. This hit arrangement can be found by finding the bin in the full parameter space with the highest value. The track candidate parameters can the be found by fetching the (θ,ρ) coordinate of the found bin.

While the preferred bin can reveal how many hits the track candidate passed through, it contains no information about which hits were contributors. However, this full parameter space was generated by summing the N parameter spaces discussed in section 1.2.2. So, the contributing hits can be readily found by looking at the same (θ,ρ) bin in each of the N parameter spaces and recording which have a non-zero value. We now have the track candidate's parameters and its contributing hits which is enough to describe the 2D trajectory.

A new search now needs to begin to find any other track candidates. However, repeating the same search of the full parameter space will return the track candidate that has already been found. To find the next track candidate, the presence of the previous track candidate must be removed. So, a reduced parameter space must be

Figure 1.11: The reduced parameter space of the 2D cluster shown in Fig. 1.7.

generated. The previous step found which of the N parameter lines contributed to the previous track candidate. So, this new parameter space can be formed by subtracting the contributing parameter lines from the full space. An example of this is shown in Fig. 1.11 where the reduced parameter space was formed by subtracting the contributing parameter lines to the highest bin in Fig. 1.10. The next track candidate can then be found by searching for the highest content bin of this reduced parameter space and said bin's contributing parameter lines.

This process can be repeated until some threshold is reached. This threshold is nominally set by demanding that at least three hits are required to form a track candidate.

1.2.4 2D track quality checks

While the approach outlined above is very powerful for recognising track-like shapes in the 2D ECal clusters, it is not capable of checking whether the selected track candidates are of sound quality. So, external checks need to be done which validate each track as it is returned from the parameter space. Fortunately, the objects returned from parameter space are simple in structure and so the quality checks can be designed to reflect this. Two necessary checks were implemented in the 2D reconstruction:

- The track can not skip a scintillator layer in a given view.

- The track can skip a maximum of 1 bar in a scintillator layer.

If a track fails either of the above conditions, the track is flagged as bad and rejected. To ensure that the same bad track is not selected in the next interaction of the parameter space analysis, the track also needs removing from the parameter space. To do this, every bin in the parameter space is checked to see if the bin is filled purely from the hits contained in the bad track. If this is the case, the bin content is set to 0.

1.2.5 3D track reconstruction

Section 1.2.3 describes the track reconstruction of a 2D ECal cluster. However, a 3D cluster consists of two sets of 2D clusters. So, the process described in section 1.2.3 must be performed on each of the 2D clusters. The result of this process is two sets of 2D tracks. To form full 3D tracks, the tracks from each view must now be matched together. This is achieved by making every pairwise comparison of the tracks from each view to find the pair which are most similar to each other. After such a pair is found, the tracks are removed from the pool and the process is repeated to find the next pair until either no tracks are left or one 2D track is left. In the latter case the single 2D track is discarded. Every pairwise combination of tracks is used to form a likelihood $\mathcal{L}$. The pair which produces the highest $\mathcal{L}$ is declared the best match and removed from the pool. Three pieces of information about the matching pair are used to calculate $\mathcal{L}$, all of which make use of probability density distributions generated using beam Monte Carlo.

As should be expected, a vertex with one visible track will have different characteristics to a vertex with three visible tracks. So, to maximise the ability of the matcher, a different set of probability density distributions are used for the 1, 2 and 3 track cases. If the number of tracks in each view is not identical, the higher number of tracks is used to find the correct probability density distributions. Separately, due to their geometrical differences, the reconstructed shape of vertices in the DS ECal will differ to those in the barrel ECals. This leads to a separate set of probability density distributions for the barrel and DS ECal modules.

The first input to the likelihood is the ratio of the total deposited charge on each track, Q_{ratio}. The denominator is taken as the track which comes from the view with the most hits. Generally speaking, a particle propagating through an ECal module

should deposit a similar amount of charge in each of the two views. So, Q_{ratio} should have a value close to 1 if the two 2D tracks are created by the same particle. An example of the Q_{ratio} distribution is shown in Fig. 1.12a, taken from beam Monte Carlo in the barrel ECals for cases where the maximum number of tracks found in a given view is 2. In Fig. 1.12a, correctly matched (in blue) shows the Q_{ratio} distribution for matching pairs which come from the same particle and incorrectly matched (in red) shows the Q_{ratio} distribution for matching pairs which were created by different particles. As Fig. 1.12a shows, Q_{ratio} well separates the two cases. To generate a probability density distribution for Q_{ratio}, the two distributions shown in Fig. 1.12a are used, but without applying any normalisation. By comparing the bins of each distribution, the probability for correctly matching two tracks in a given bin p_i can be formed by

$$p_i = \frac{s_i}{s_i + b_i},\tag{1.9}$$

where s_i is the number of correctly matched tracks in bin i and b_i is the number of incorrectly matched tracks in bin i. A discreet probability density distribution for Q_{ratio} can then be formed by calculating p_i for every bin. The discreet probability density distribution is then interpolated with splines to create the final probability distribution. An example of this for the two track, barrel case is shown in Fig. 1.12b. When a matching candidate pair is being considered, the value of Q_{ratio} is calculated and used in the spline to retrieve $\mathcal{L}_{Q_{\text{ratio}}}$.

The second input to the likelihood, called $\Delta_{\text{layer, first}}$, is the difference in the starting layer of each 2D track which forms the matching candidate pair, where starting layer refers to the layer closest to the ND280 tracker. For 2D tracks which should be matched together, $\Delta_{\text{layer, first}}$ should be 1. The separation ability of this variable for the two track, barrel is shown in Fig. 1.13a. The discreet probability density function was created using eqn. 1.9. It was not necessary to interpolate using splines as $\Delta_{\text{layer, first}}$ is itself discreet. The probability density function for $\Delta_{\text{layer, first}}$ is shown in Fig. 1.13b for the two track, barrel case. For each matching candidate pair, the value of $\Delta_{\text{layer, first}}$ is calculated and the corresponding $\mathcal{L}_{\Delta_{\text{layer, first}}}$ is retrieved from the probability density function.

The third and final input to the likelihood, called $\Delta_{\text{layer, last}}$, is the difference in the ending layer of each 2D track which forms the matching candidate pair, where the ending layer refers to the layer furthest from the ND280 tracker. Functionally, how
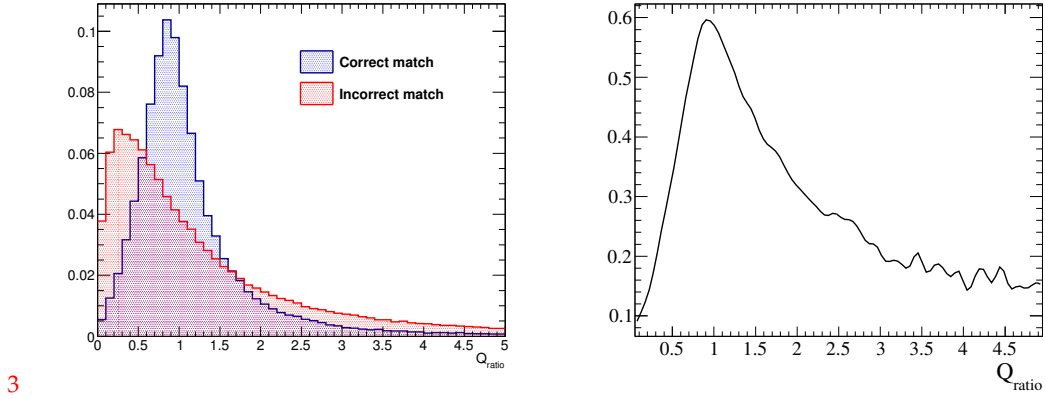
(a) Q_{ratio} distribution (area normalised). The blue and red distributions refers to matching pairs which were matched to the same true particle and different true particles respectively. The two distributions peak at different values of Q_{ratio}, which implies Q_{ratio} provides good separation of the correctly and incorrectly matched events.

(b) Q_{ratio} probability density distribution. The peak of the distribution aligns well with the correct matches peak in Fig. 1.12a which aides in maximising the number of correct matches made.

Figure 1.12: Q_{ratio} and its probability density distribution in the barrel ECal for the two track case. NEUT-based simulation of ND280 beam events were used to produce the distributions.

this function is used is essentially identical to $\Delta_{\text{layer, last}}$ so it will not be described in detail. The separation ability of this variable and its corresponding probability density function for the two track, barrel case are shown in Fig. 1.14a and Fig. 1.14b respectively.

The matching likelihood, $\mathcal{L}$, for a matching candidate pair is then

$$\mathcal{L} = \mathcal{L}_{Q_{\text{ratio}}} \times \mathcal{L}_{\Delta_{\text{layer, first}}} \times \mathcal{L}_{\Delta_{\text{layer, last}}}. \tag{1.10}$$

As described bove, $\mathcal{L}$ is calculated for every matching candidate pair and the pair which maximise $\mathcal{L}$ is selected as a match and removed from the pool. The process is then repeated until no more matches can be made.

3D tracks have now been formed, but the associated directions and positions of those tracks still need to be calculated. The track fitting process for the newly formed 3D tracks is very similar to that described in section **??**. The tracks are briefly separated into their constituent 2D views and a charge-weighted average position of each layer
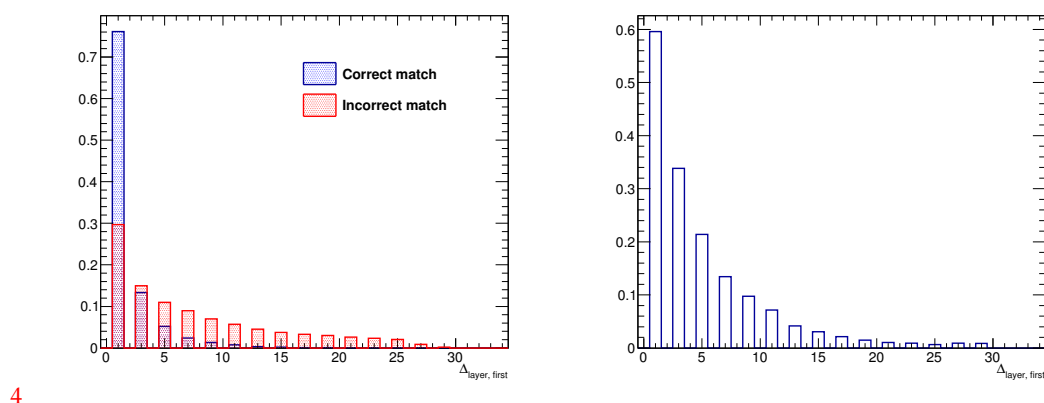
4

(a) $\Delta_{\text{layer, first}}$ distribution (area normalised) The blue and red distributions refers to matching pairs which were matched to the same true particle and different true particles respectively. While both distributions peak in the same place, the peak for the correct matches distribution is much sharper, indicating a good level of separation between the correctly and incorrectly matches events.

(b) $\Delta_{\text{layer, first}}$ probability density distribution. The peak of the distribution aligns well with the correct matches peak in Fig. 1.13a which aides in maximising the number of correct matches made.

Figure 1.13: $\Delta_{\text{layer, first}}$ and its probability density distribution in the barrel ECal for the two track case. NEUT-based simulation of ND280 beam events were used to produce the distributions.
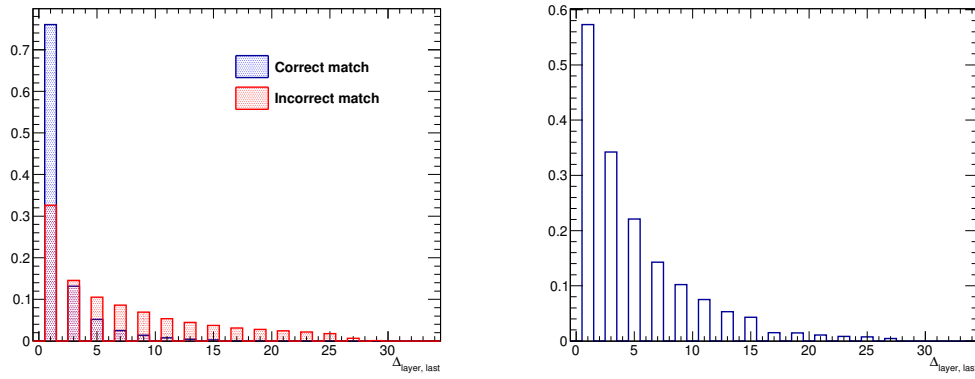
(a) $\Delta_{\text{layer, last}}$ distribution (area normalised). The blue and red distributions refers to matching pairs which were matched to the same true particle and different true particles respectively. While both distributions peak in the same place, the peak for the correct matches distribution is much sharper, indicating a good level of separation between the correctly and incorrectly matches events.

(b) $\Delta_{\text{layer, last}}$ probability density distribution. The peak of the distribution aligns well with the correct matches peak in Fig. 1.14a which aides in maximising the number of correct matches made.

Figure 1.14: $\Delta_{\text{layer, last}}$ and its probability density distribution in the barrel ECal for the two track case. NEUT-based simulation of ND280 beam events were used to produce the distributions.
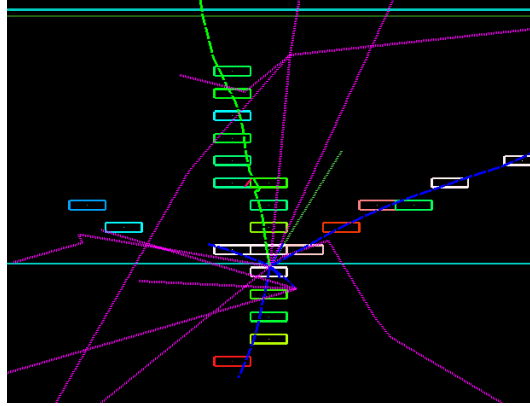
Figure 1.15: Event display of a problematic (for the reconstruction) neutrino interaction in the ECal. The solid green track is the muon, the solid blue tracks are protons and the pink tracks are neutrons. The neutrino is the short dashed green line.

is calculated using the track's constituent hits. Then, the hits in the opposing view are used to estimate the third coordinate of a given layer using a least-squares fit. After all of the coordinates have been estimated, a full 3D least-squares fit of the positions in each layer is performed to estimate the 3D track's direction and position in that ECal layer.

1.2.6 Track splitting

During development of the reconstruction, it became clear that a certain topology had been overlooked. An example of this is shown in Fig. 1.15 which shows a MC neutrino interaction in the ECal with 3 charged final states. As can be seen from Fig. 1.15, the muon (solid green line) is emitted back-to-back with one of the final-state protons (solid blue line) in this ECal view. Because the Hough transform implementation only concerns itself with straight lines, the result is that such back-to-back trajectories are typically reconstructed as a single track. However, there are two views available for every ECal module and the back-to-back emittance typically only appears in the ECal view which is perpendicular to the beam direction (the XY view). So, the correctly reconstructed tracks in the other ECal view can be used to split the tracks in the problematic view.

Consider a neutrino interaction with two charged final-states which has been reconstructed as one track in one view (called the merged view) but reconstructed as two tracks in the other view (called the other view). It should be expected that the single

track in the merged view is not a particularly good match for either of the tracks in the other view. However, if the two tracks in the other view were temporarily merged together and this new track was compared to the single track in the merged view, one should expect this match to return a much higher value of $\mathcal{L}$. This feature can be used to identify a potentially merged track in a given view.

This motivated an extension to the 3D matching aspect of the reconstruction. As a reminder, the 3D matching algorithm makes every pairwise comparison of tracks from each view to find the pair which maximise $\mathcal{L}$. This matching routine was modified to also include temporary mergings of every pairwise combination of tracks in a single view. These temporary mergings can then be compared to every single track in the other view. As an example, consider a situation where 3 tracks (labelled A, B and C) have been reconstructed in one view and two tracks (labelled Y and Z) have been reconstructed in the other view. With the old method, the following comparisons would be made:

$$
\begin{aligned}
A &\longleftrightarrow Y \\
A &\longleftrightarrow Z \\
B &\longleftrightarrow Y \\
B &\longleftrightarrow Z \\
C &\longleftrightarrow Y \\
C &\longleftrightarrow Z
\end{aligned}
\tag{1.11}
$$

With the new method, which includes temporarily merged pairs of tracks in a given view, the following comparisons would be made:

$$
\begin{aligned}
A &\longleftrightarrow Y \\
A &\longleftrightarrow Z \\
B &\longleftrightarrow Y \\
B &\longleftrightarrow Z \\
C &\longleftrightarrow Y \\
C &\longleftrightarrow Z \\
A + B &\longleftrightarrow Y \\
A + B &\longleftrightarrow Z \\
A + C &\longleftrightarrow Y \\
A + C &\longleftrightarrow Z \\
B + C &\longleftrightarrow Y \\
B + C &\longleftrightarrow Z \\
A &\longleftrightarrow Y + Z \\
B &\longleftrightarrow Y + Z \\
C &\longleftrightarrow Y + Z
\end{aligned}
\tag{1.12}
$$

In terms of the matching comparisons, the temporarily merged comparisons are treated on the same footing as the single track comparisons; $\mathcal{L}$ is calculated for each comparison and the one which maximises $\mathcal{L}$ is selected. However, the post-matching treatment of the best match depends on whether a temporary merge is involved. If the match which maximises $\mathcal{L}$ involves two single tracks then the treatment is as before; they are removed from the pool and the process is repeated. If a temporarily merged pair are involved, the 2D crossing location of the temporarily merged tracks is calculated and is then used to split the single track in the other view. The original track is removed from the pool and replaced by the two single tracks formed from the split. The matching process is then begun again and repeated until all matches have been made.

1.2.7 Track pairwise crossing reconstruction

The final step of the reconstruction is to estimate where each of the 3D track's paths cross. As each track is reconstructed as a straight line in 3D, the final step is fairly simple. Using the track direction and position information calculated at the end of section 1.2.5, the position at closest approach for every pairwise combination of 3D tracks is calculated analytically. The distance of closest approach is also calculated. Six hits, the closest three from each 3D track, are then associated to the pairwise crossing.

1.3 Output of the reconstruction

The reconstruction is run over every 3D cluster found in the ECal. By applying the steps outlined above, for each 3D cluster the following output is given:

- A set of 3D tracks

- The pairwise crossings of all 3D tracks found in the cluster

Note that no vertex formation beyond the pairwise crossings is calculated at this stage, nor is any analysis of the 3D tracks performed. While this may seem like an oversight of the reconstruction, this approach was decided as no assumptions are made about what the tracks/crossings represent at this point, making the output more generic. Any analysis which wants to make use of the reconstruction is given enough information to apply more targeted reconstruction downstream.

1.4 Validation of the reconstruction

Because of the large scope of the reconstruction and the limited time available for the presented analysis, the validation of the reconstruction was done in parallel to the rest of the analysis and is still an ongoing effort. The validation that has been done can be split into two areas: validation of the performance of the algorithms purely using MC and comparisons of MC to data using control samples.
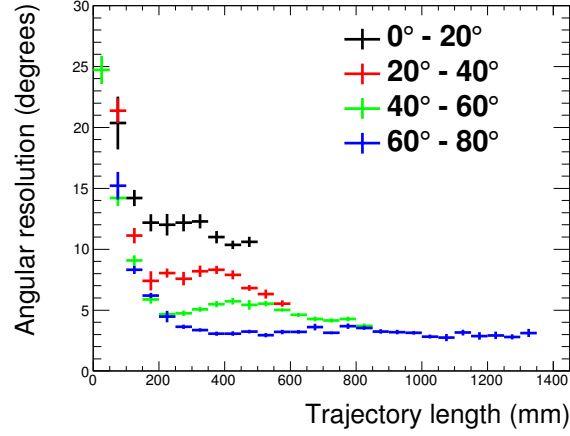
Figure 1.16: The angular resolution as a function of trajectory length in the DS ECal when applying the enhanced reconstruction to muon MC. The colour coding refers to the true entry angle range of the muons.

1.4.1 Validation of algorithm performance

The first performance validation investigated the angular resolution using the enhanced reconstruction (by L. Pickering). This study calculated the angular resolution for MC muons fired into the side-left ECal for a range of entry angles. For each MC event, the cosine of the angular separation between the true particle angle and the reconstructed angle was calculated, $\cos \theta^{\text{Sep}}$. The values of $\cos \theta^{\text{Sep}}$ were then binned in a distribution. An outward scan from the peak of the distribution was then performed to find where the height decreased to 68% of the peak. The value of θ^{Sep} and this point was taken as the angular resolution. These results are shown in Fig. 1.16. Generally speaking, the found angular resolutions are very good. For long trajectories (200 mm), the angular resolution is within 15°. It is only for short tracks (40 mm) that the angular resolution becomes large.

The second performance validation studied the success of the 3D matching. To do this, a sample of beam MC events in the ECals were processed through the enhanced reconstruction. After completion, the 2D components of the 3D tracks were analysed and matched to the true particles which created them. A match was counted as a success if both 2D components were matched to the same true particle. These results are shown in table 1.1, separated out by which track matching likelihood was used. For the 1 and 2 track likelihood cases, the matching performs very well. It is only in cases where the 3 track likelihood is used that the matching start to suffer slightly.

	1 track likelihood	2 track likelihood	3 track likelihood
1st track matched	96%	92%	80%
2nd track matched		89%	79%
3rd track matched			70%

Table 1.1: The percentage number of correct matches in the 3D matching separated by which track matching likelihood was used.

However, all of the correct matching rates are well above 50% which suggests that the 3D matching is performing adequately.

1.4.2 Data-motivated validation of the algorithms

As described above, the validation is still an ongoing effort and, so far, all of the data-motivated validation has been done by L. Pickering. At time of writing, validation events measured in ND280 can be split into two groups:

1. **FGD collinear cosmics (named fgdcol):** A sample of clean FGD-triggered cosmic events which are scaled to have an equal distribution of angles.

2. **Through-going basket muons (named bskmu):** A sample of clean beam-triggered events which solely contain a muon depositing energy in TPC2, TPC3 and the DS ECal.

The fgdcol sample will naturally contain a good sample of barrel ECal events whilst having only a limited number of DS ECal events whereas the reverse is true for the bskmu sample. So, it follows that the fgdcol and bskmu samples should be used to separately assess the reconstruction in the barrel ECal and DS ECal respectively.

Fig. 1.17 shows the summed charge contained in all tracks reconstructed in each ECal cluster. To clarify what this means, if a reconstructed ECal cluster contained three reconstructed tracks where tracks 1, 2 and 3 contain 20 MEU, 50 MEU and 30 MEU of charge respectively, that event would be registered as having 100 MEU of charge in the relevant distribution in Fig. 1.17. Both the barrel ECal and DS ECal samples show a large discrepancy around the charge peak. This offset can be explained as a hit-level charge discrepancy between data and Monte Carlo and is not caused by the

(a) Barrel ECal events in the fgdcol sample.

(b) DS ECal events in the bskmu sample.
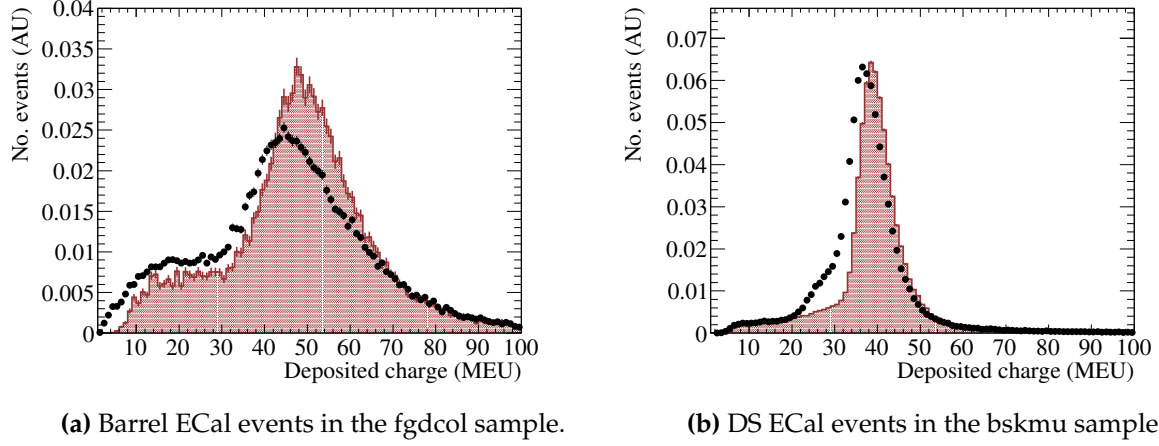
Figure 1.17: The summed charge contained on all tracks reconstructed in each ECal cluster. The red histograms and black points are Monte Carlo and data respectively.

reconstruction. This discrepancy should, however, be considered during analysis of the systematic uncertainties. Unfortunately, the DS ECal events in the bskmu sample (Fig. 1.17b) shows an extra data excess in the 20 MEU to 30 MEU region which is just before the charge peak. This data excess can not be explained by a relative hit inefficiency.

Fig. 1.18 shows the summed number of hits contained in all tracks reconstructed in each ECal cluster. Generally speaking, the distributions in Fig. 1.18 share similar features to those in Fig. 1.17. Importantly, an excess of data events appears just before the peak in Fig. 1.18. The fact that this excess also appears in Fig. 1.18 strongly suggests that the issue is caused by the number of hits associated to the reconstructed tracks, rather than the deposited charge. Further investigation of this discrepancy revealed that a mismodelled hit inefficiency, most likely due to dead DS ECal channels, was the issue. One of the 2D track quality checks (see section 1.2.4) requires that a 2D track candidate can not skip a layer in a given view which is problematic when considering dead channels.

To test this hypothesis, this requirement was relaxed to allow a 2D track candidate to skip a single ECal layer and the Monte Carlo bskmu sample was re-processed. The re-processed DS ECal events are shown in Fig. 1.19. As can clearly be seen, the data excess before the peak in the distributions has now gone. Unfortunately, large scale processing and analysis of beam Monte Carlo events had already started by the time this issue was discovered and so it was infeasible to include this bug fix in the

(a) Barrel ECal events in the fgdcol sample.   **(b)** DS ECal events in the bskmu sample.
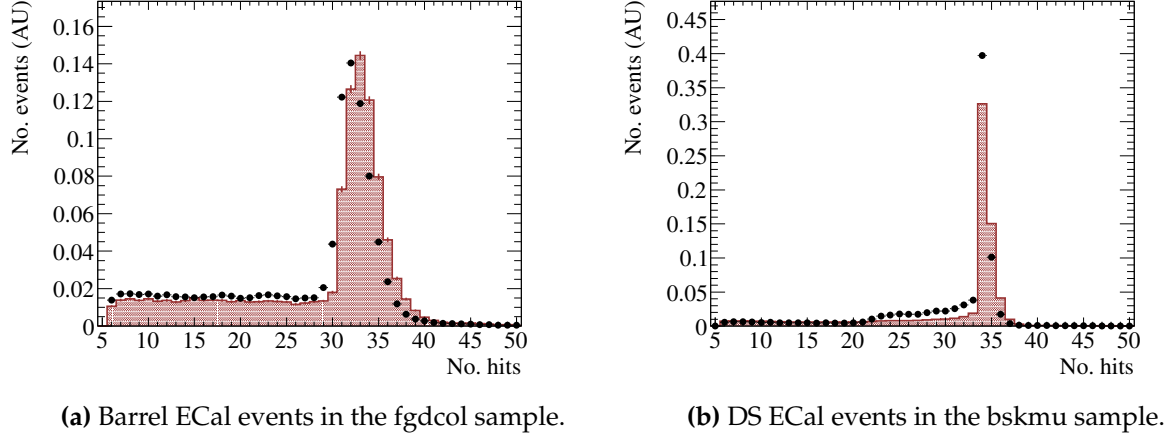
Figure 1.18: The summed number of hits contained on all tracks reconstructed in each ECal cluster. The red histograms and black points are Monte Carlo and data respectively.

analysis. So, it was decided that this issue would be treated as an additional systematic uncertainty. The collected data events were processed with this fix in place.

(a) Summed charge contained on all tracks in each reconstructed ECal cluster.   **(b)** Summed number of hits contained on all tracks in each reconstructed ECal cluster..
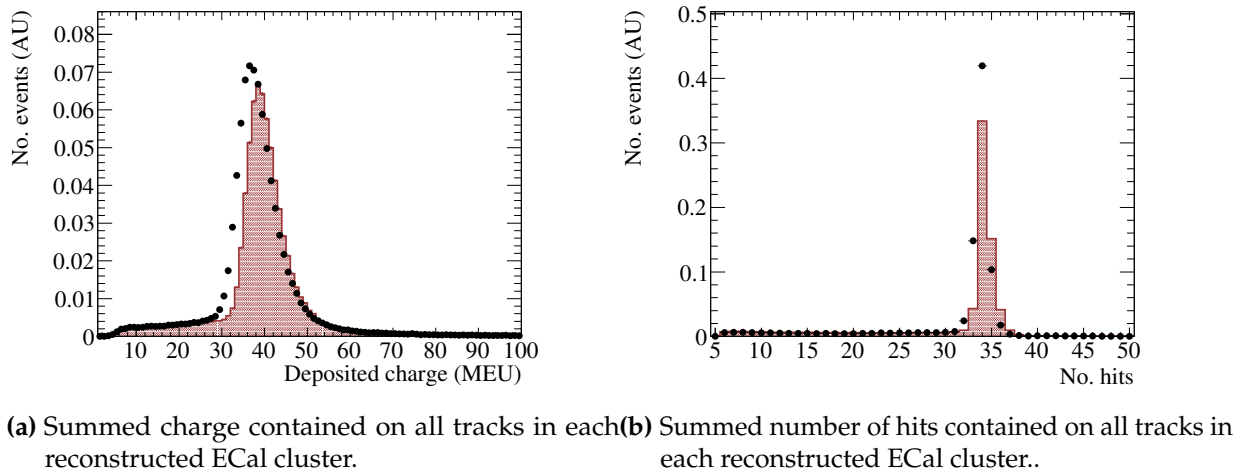
Figure 1.19: The number of DS ECal events in the bskmu sample after relaxing the 2D track quality check. The red histograms and black points are the Monte Carlo and data respectively.

Chapter 2

Magnetic field simulation in ND280

ND280 is housed in the former[1] UA1 magnet which provides a 0.18[2] T magnetic field through the basket. The purpose of this magnetic field is to aid particle identification[3] and momentum measurements[4] in ND280's TPCs. This magnetic field is accurately modelled in nd80mc by a constant 0.18 T magnetic field in the basket. The ND280 analyses, which are inputs to the oscillation analyses, search for a TPC track matched to an FGD track so, in a first iteration of these analyses, the magnetic field model is sufficient for its purpose.

However, a significant part of the UA1 magnet is the iron based, magnetic flux return yoke which helps to tightly contain the magnetic field outside of the tracker region. As a result, there is a significant magnetic field contained within the magnetic flux return yoke during operation. This magnetic field in the flux return yoke is not modelled in nd280mc. For the first iterations of the ND280 oscillation input analyses, this approximation was valid. However, as the ND280 analyses become more mature, and non-tracker based analyses are started, this approximation is no longer sufficient. So, the magnetic field model in the simulation needs revising.

The Monte Carlo event rates seen in the ECals are directly affected by mismodelling of the magnetic field in the yokes which can have serious consequences for any ECal based analysis. So, the following chapter presents the first investigation of the magnetic field's effect in this region and an improvement to the magnetic field model. This model

---

[1] it isn't the UA1 magnet any more!
[2] It's not a 0.2 T field any more!
[3] was identifcation
[4] not just PID
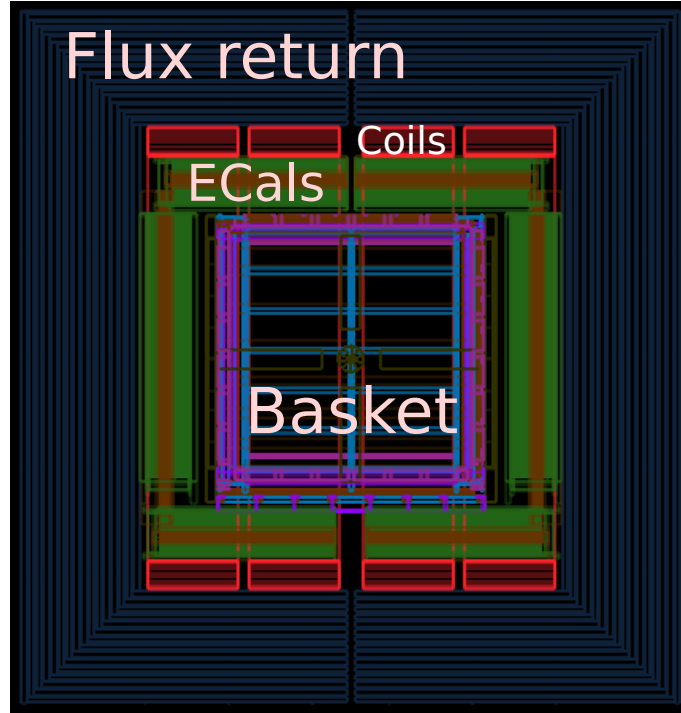
Figure 2.1: Graphical display of the X-Y ND280 cross-section.

improvement has now been incorporated into the official ND280 MC simulations and is now used by all physics analyses at ND280.[5]

2.1 Magnetic field model in the ND280 flux return

A simple model for the magnetic field in the flux return can be found by making two assumptions. Firstly, the flux return yoke consists mostly of iron which has a much higher magnetic permeability than the air surrounding it. So, it can be assumed that any magnetic flux passing through the ND280 basket is solely transported back around by the return yoke (no flux passes through the atmosphere in the pit). It follows that

$$\phi_b = \phi_r, \tag{2.1}$$

---

[5]I would add something like "As one of the analysers who has been central to studying events occurring in the ECals, which are directly affected by mismodelling of the magnetic field in the yokes, I was the first T2K collaborator to investigate this effect and provide an improved field model; this was subsequently adopted as the field to be used in official ND280 MC simulations, used by all physics analyses at ND280.
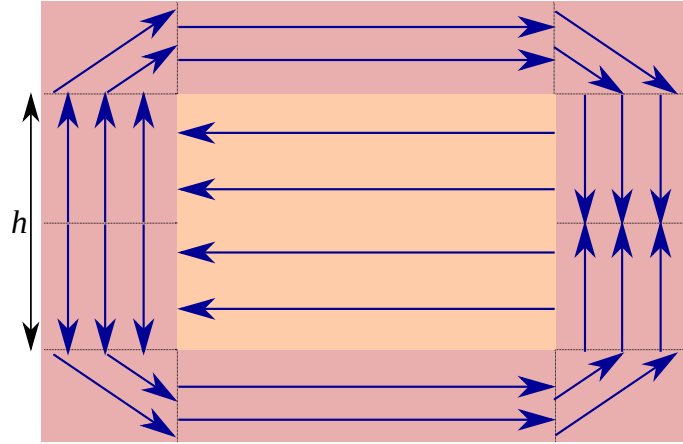
Figure 2.2: Simple model of the magnetic field in the basket and flux return region. The flux return yoke has been separated into ten sections: four vertical B field sections, four corner B field sections and two horizontal B field sections. The height of the basket region, h, is also shown.

where ϕ_b is the magnetic flux passing through the tracker and ϕ_r is the magnetic flux passing through the return yoke. The second assumption regards the shape of the ND280 basket and flux return yoke. The X-Y cross-section of ND280, as shown in Fig. 2.1, can be modelled as two distinct parts: the flux return yoke and everything contained within. It is clear from Fig. 2.1 that both areas are rectangular[6] so the system can be modelled as a smaller rectangle (the basket) contained within a larger rectangle (the return yoke). Using this assumption and Eq. 2.1, the magnetic field strength passing through the return yoke, B_r, is

$$B_r = \frac{B_b A_b}{A_r - A_b},$$ (2.2)

where B_b is the strength of the magnetic field passing through the basket, A_b is the cross-sectional area of the basket region and A_r is the cross-sectional area of the flux return yoke if the flux return yoke was not hollow.

Eq. 2.2 is sufficient to model the strength of the magnetic field in the flux return yoke, yet Eq. 2.2 conveys no information about the direction of the magnetic field. However, the direction can be estimated by separating the flux return into ten sections as shown in Fig. 2.2. The sections are: four vertical sections where the magnetic field enters and exits the flux return region, two horizontal sections where the magnetic field in the flux return is anti-parallel to the magnetic field in the basket and four cor-

---

[6]retangular

ner sections where the magnetic field transitions between the horizontal and vertical sections. By defining the magnetic field in the basket to be parallel to the *x*-axis

$$\vec{B_b} = B_b \hat{\imath},$$
(2.3)

where $\imath$ is the unit vector in the *x* direction[7] then it follows that the horizontal magnetic field in the flux return is

$$\vec{B}_r^H = -B_r \hat{\imath}.$$
(2.4)

The field model for the vertical section should take into account that the strength of the magnetic field is not constant, but increases in strength until it reaches the corner region[8]. The direction of the field depends on which vertical section is under consideration. For the section where[9] the magnetic field is exiting the tracker and moving upwards, the relevant vector is

$$\vec{B}_r^V = \frac{y}{h/2} B_r \hat{\jmath},$$
(2.5)

where h is the height of the ND280 basket and y is the height at which the magnetic field is being evaluated in the ND280 coordinate system. In the corner regions, the magnetic field is defined to be straight, constant in strength and at $45°$ to the horizontal and vertical sections. As with the vertical section, the magnetic field direction is dependent on which corner section is being considered. For the corner section where the magnetic field is exiting the tracker and travelling vertically upwards (as defined in Eq. 2.5), the vector is

$$\vec{B}_r^C = \frac{B_r}{\sqrt{2}} (\hat{\jmath} - \hat{\imath}).$$
(2.6)

The magnetic field in the other corner sections are then $45°$ rotations of Eq. 2.6.

---

[7]need to define stuff properly.

[8]What is the corner section? And reaching it from which direction?

[9]can this be explained graphically? It's hard to follow what you mean. It's not absolutely needed, but it would make it easier for the reader...

(a) Number of hits in the reconstructed cluster.

(b) The truncated max ratio of the reconstructed cluster.
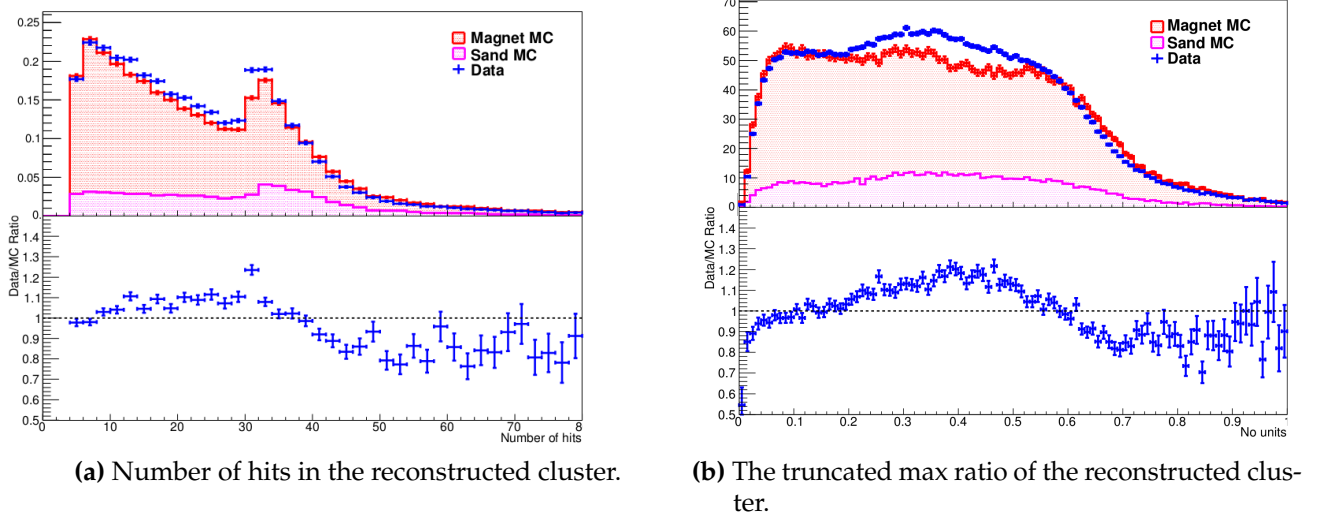
Figure 2.3: Comparisons of data and Monte Carlo in the bottom-left barrel ECal for previous software productions. The red and pink histograms are Monte Carlo simulation of T2K beam neutrinos incident on ND280 and the surrounding pit respectively. The blue data points are collected data from run 3C. Both of the plots are POT normalized.

2.2 Effect of magnetic field on the ECal

It was found in previous iterations of ND280 analyses that there were significant discrepancies between the Monte Carlo and the collected data in the ECal. The discrepancies found had an ECal module dependence where the bottom modules were affected most. The problem appeared in the low-level distributions, such as how many scintillator hits were assigned to each reconstructed object. An example of this is shown in Fig. 2.3a which shows a comparison of Monte Carlo with run 3C data for the number of constituent hits in each reconstructed object measured in the bottom-left barrel ECal. For the number of hits region with high population (between roughly 10 and 30) there is a clear excess of collected data events. As the high level variables, such as the ones used for track-shower discrimination, are based on these low-level quantities, the discrepancy propagated through causing significant disagreement at all levels. An example of this effect is shown in Fig. 2.3b which shows a data and Monte Carlo comparison, again for the bottom-left barrel ECal, for the Truncated Max Ratio (TMR) of the reconstructed objects. The TMR, which calculates the ratio of the lowest total charge found in an ECal layer to the high total charge in an ECal layer after removing the top and bottom 20% of hits, is an input into the track-shower

(a) Number of hits in the reconstructed cluster.

(b) The truncated max ratio of the reconstructed cluster.
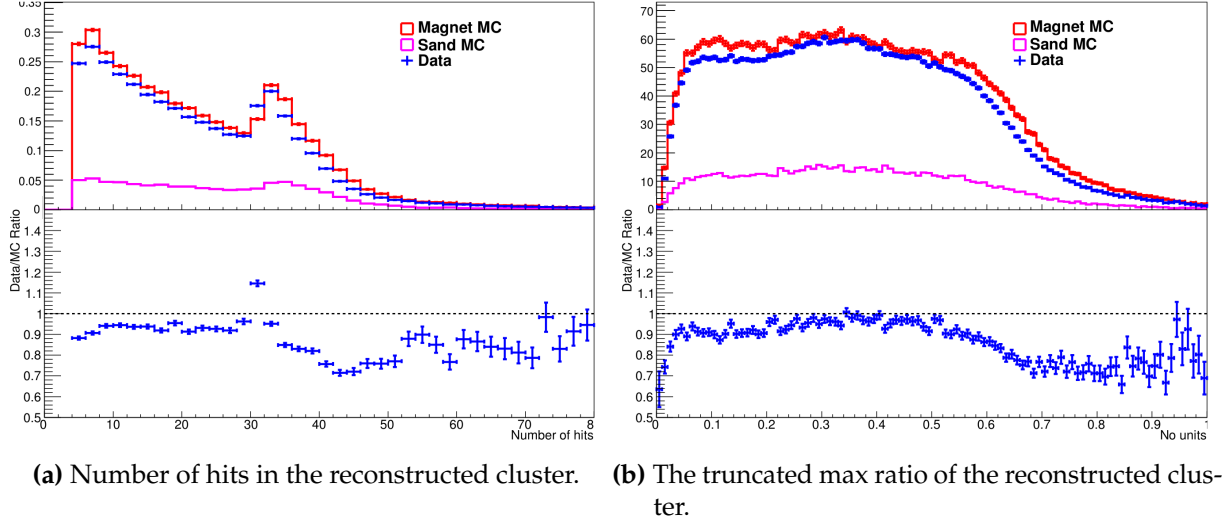
Figure 2.4: Comparisons of data and Monte Carlo in the bottom-left barrel ECal with the magnetic field model described in section 2.1 implemented. The red and pink histograms are Monte Carlo simulation of T2K beam neutrinos incident on ND280 and the surrounding pit respectively. The blue data points are collected data from run 3C. Both of the plots are POT normalized.

discriminator described in section **??**. The track-shower discrimination is a key feature of the ECal reconstruction which is used by several ND280 analyses so such a big discrepancy is a serious problem.

As ND280 is off-axis relative to the T2K beam, there is an increase in the neutrino flux in the flux return yoke and surrounding pit regions below the bottom ECals. This means that any charged final states in this region would generally have to propagate through the flux return yoke. If a magnetic field is present in this region, as there would be during data taking, the trajectory of such particles would be bent upwards towards the ND280 tracker region, causing an increase in the event rate in the bottom ECals. If the magnetic field in this region is missing, the above statement does not hold and a relative deficit of events would be seen which describes the situation seen in Fig. 2.3. So, the simple magnetic field model in the flux return yoke described in section 2.1 was implemented in nd280mc and a batch of beam and sand Monte Carlo[10] was produced to test its effect. To get an idea of the magnetic field's effect on the rates measured by the ECals, the same variables as shown in Fig. 2.3 are shown in Fig. 2.4, but with the magnetic field activated. The difference is very clear; Fig. 2.4a shows that

---

[10]"sand Monte Carlo" is very much jargon. Introduce it properly

the excess in the 10 to 30 hits region is now gone. It is also clear that the effect of the magnetic field has propagated through to the high level discriminators, as shown in Fig. 2.4b.

Despite this study only briefly investigating the presence of a magnetic field in the UA1 flux return yoke, the improvement provided is undeniable. It was decided that the model would be a permanent feature of the ND280 simulation and is now used in all software productions including the inputs to this analysis.

Bibliography

[1] P. a. Hough, Conf.Proc. **C590914**, 554 (1959).

[2] R. O. Duda and P. E. Hart, Commun. ACM **15**, 11 (1972).

[3] J. Vuillemin, Fast linear hough transform, in *Application Specific Array Processors, 1994. Proceedings. International Conference on*, pp. 1–9, 1994.

List of Figures

List of Tables